Analysis and Suppression Strategy of Synchronous Frequency Resonance for Grid-Connected Converters With Power-Synchronous Control Method

Xiaoling Xiong, *Member, IEEE*, Yan Zhou, Bochen Luo, Peng Cheng, *Member, IEEE*, and Frede Blaabjerg, *Fellow, IEEE*

***Abstract*—The power-synchronization control (PSC) method of grid-connected converters, which is based on the active power orientation, is a promising solution for high-penetration renewable power generation systems. Unfortunately, synchronous frequency resonance (SFR) is inevitably found in PSC-controlled converters, especially when connected to inductive networks, which seriously damages the stability of the system. The relatively small equivalent resistance of the inductive network is regarded as the main cause of SFR, and a virtual resistor (VR) is usually employed to dampen this kind of oscillation. However, another important reason for SFR is the nonminimum phase effect of the loop gains, which is discussed in this article. Considering the dynamics of the grid equivalent inductance, the small-signal model of PSC-controlled converter is established. By this, the mechanism of SFR and the nonminimum phase effect are revealed. Furthermore, a conjugate poles elimination control method based on auxiliary branches introduced into the power control loops is proposed to suppress SFR, which can also broaden the control bandwidth compared with the VR method. Finally, the theoretical analysis is verified by simulations and hardware-in-loop experimental results.**

***Index Terms*—Grid-forming converter, power-synchronous control, synchronous frequency resonance (SFR) suppression, voltage source converter (VSC).**

I. Introduction

THE increase in renewable power resources is continuously integrated into power grids through voltage source converters (VSCs) in recent years. The grid-connected VSCs are widely employed as an important interface device between new energy generation and the power grid [1], which is mainly divided into grid-following VSCs and grid-forming VSCs based on their different synchronization methods [2].

The vector-current-controlled grid-following VSCs are the dominating method in numerous applications, which regulate the instantaneous power through a fast inner current control loop. To maintain synchronization with the grid, a phase-locked loop (PLL) is usually adopted in grid-following VSCs to detect the accurate frequency and phase of the grid, i.e., the point of common coupling (PCC) voltage [3], which works well as long as the PCC voltage is stiff. However, the real grid is becoming weaker and weaker as the renewable energy penetration, and power electronic-based devices are increasing more in the grid [4]. Under this weak grid condition, the real PCC voltage varies a lot with the different injected currents to the grid, which seriously damages the stability of grid-following VSCs, due to the significant negative resistance effect of the PLL [5], [6], [7]. Moreover, the grid-following VSCs operate as a current source, which cannot directly support the voltage and frequency for the loads [8]. These issues limit the further increase of the renewable power penetration scale into the grid.

In order to improve the stability of the power system dominated by power electronic devices, the concept of grid-forming VSCs was proposed in [9]. In contrast to grid-following VSCs, grid-forming VSCs synchronizes with the grid based on active power orientation, which is a family of control schemes where the operation of synchronous generators (SG) is emulated, such as virtual synchronous generator (VSG) control [10]. In most literature, the dynamics of the grid equivalent inductance are ignored, then the outer-loop controlled VSG is regarded as a second-order system due to the virtual inertia block. A large active power droop coefficient, the reciprocal of which corresponds to a small damping coefficient, may lead to low-frequency oscillations, i.e., subsynchronous oscillations in [11] and [12]. The extra damping torque with auxiliary control methods needs to be added to dampen this kind of low-frequency oscillation [13], [14].

Different from the objective of VSG, the PSC method is proposed in [15], which also belongs to the grid-forming control family, but aims to stabilize the grid-connected VSCs, not to provide virtual inertia. Since then, the power-synchronization control (PSC) strategy has been widely used in different applications, such as long-distance transmission systems [16],

Manuscript received 28 July 2022; revised 26 December 2022; accepted 20 January 2023. Date of publication 31 January 2023; date of current version 20 April 2023. This work is supported in part by the National Key Research and Development Program of China under Grant 2021YFB2601602 and in part by National Natural Science Foundation of China under Grant 52277176. Recommended for publication by Associate Editor M. Molinas. *(Corresponding author: Xiaoling Xiong.)*

Xiaoling Xiong, Yan Zhou, and Bochen Luo are with the State Key Laboratory of Alternate Electrical Power System with Renewable Energy Sources, North China Electric Power University, Beijing 102206, China (e-mail: xiongxl1102@ncepu.edu.cn; zhouyan2020@ncepu.edu.cn; luobochen2021@ncepu.edu.cn).

Peng Cheng is with the China Institute of Energy and Transportation Integrated Development, North China Electric Power University, Beijing 102206, China (e-mail: p.cheng@ncepu.edu.cn).

Frede Blaabjerg is with the Department of Energy, Aalborg University, 9220 Aalborg, Denmark (e-mail: fbl@et.aau.dk).

Color versions of one or more figures in this article are available at https://doi.org/10.1109/TPEL.2023.3240623.

Digital Object Identifier 10.1109/TPEL.2023.3240623

weak-grid applications [17], [18], and renewable power resources interface converters [19], [20]. If ignoring the dynamics of the grid inductance, a PSC-controlled VSC can be regarded as a first-order system. In this way, low-frequency oscillations will not occur. However, the dynamics of the grid equivalent inductance do have an impact on the low-frequency stability of the PSC-controlled VSC, which is called synchronous frequency resonance (SFR). SFR only occurs in the power control loops of grid-forming converters due to the dynamics of the grid inductance, which has been first reported in [15] and further studied in [21] and [22].

When the dynamics of the grid inductance are considered, it is found that a pair of conjugate poles exist in the open-loop gains, which is related to the equivalent grid resistance and inductance. This pair of poles will introduce a resonance peak and cause $-180°$ phase jump around the synchronous frequency. Thus, it might trigger an oscillation in the output power of the converter. Since the frequency of the oscillation is around the synchronous frequency, this phenomenon is, thus, called SFR in [15]. SFR is a great threat to the stable operation of the power system [23], [24]. Several papers have shown that the relatively small equivalent resistance of the inductive network is the main cause of SFR. Yet, the other reasons have been rarely investigated.

To dampen SFR, a virtual resistor (VR) is usually employed without introducing power loss [14]. Yet, adding a VR enlarges the ratio of the equivalent resistance to the equivalent reactance of the system. As a result, the coupling effect between the active power control loop (APCL) and the reactive power control loop (RPCL) is increased [25], making it more difficult to control them independently. Meanwhile, the VR may reduce the active power transfer capability and narrow the stability region of the system [26]. A phase-amplitude cross-regulation scheme is proposed to remove the resonance peaks for VSG in [25]. However, the power angle for power transfer is relatively small, and in other words, it is designed for light or small active power injected into the grid, which cannot be satisfied under most conditions. As a usually used method for analyzing the stability of VSCs, the small-signal model can accurately reflect the low-frequency dynamics of the system around the equilibrium point and is also helpful for understanding the physical mechanism. Therefore, a generalized small-signal model for PSC-controlled converters should be developed, and the mechanism of SFR should be investigated thoroughly. An SFR suppression method considering a wide power range is also required.

This article is going to solve the aforementioned problems, and the main contributions can be summarized as following.

1) A small-signal model for a PSC-controlled grid-connected converter considering the dynamics of the grid equivalent inductance is established, and a mathematical model considering the coupling effect between APCL and RPCL is derived. Through them, it is found that not only the small equivalent resistance of the grid but also the nonminimum phase effect of the loop gains is the main important cause for SFR.
2) In order to suppress SFR of the PSC-controlled converter and enhance the stability, a conjugate poles elimination control method based on auxiliary branches introduced into the power control loops is proposed. This method can not only eliminate the conjugate resonant poles in the open-loop gains of APCL and RPCL, but can also remove the nonminimum phase effect in the power control loops, resulting in the stability of the system being greatly improved.
3) Compared with the VR method, the proposed conjugate poles elimination method can suppress the SFR and also effectively broaden the power loop's control bandwidth, improving the system's dynamic response and making it adaptive to a wider range of system parameters.

The rest of this article is organized as follows. The configuration and small-signal model of the PSC-controlled grid-connected converter is presented in Section II, by which the mechanism of SFR, i.e., the nonminimum phase effect, is revealed. To suppress SFR, a conjugate poles elimination control method based on auxiliary branches introduced into the power control loops is proposed in Section III, which also provides a design-oriented process of the proposed method. The theoretical analysis is validated by simulation and hardware-in-loop experimental results in Section IV. Finally, Section V presents the conclusion.

II. Mechanism of SFR in PSC-Controlled Grid-Connected Converter

A. Configuration of PSC-Controlled Grid-Connected Converter

The topology and control block diagram of the PSC-controlled grid-connected converter is shown in Fig. 1. The converter is connected to the PCC through a filter, which consists of L_f and C_f. R_g and L_g represent the equivalent resistance and inductance for the grid. $\mathbf{V_g} = V_g e^{j\omega_g t}$ (the angular frequency ω_g is usually equal to the rated angular frequency ω_0) and $\mathbf{V_{pcc}} = V_{pcc} e^{j\theta_{pcc}}$ represent the space vectors for the grid voltage and the PCC voltage, respectively. $\mathbf{I_g}$ is the space vector of the current injected into the grid at the PCC. P_{out} and Q_{out} are the output active and reactive power at the PCC. Moreover, the low-pass filter is used to filter out the high-frequency power fluctuations in P_{out} and Q_{out}, in which ω_c is the cut-off frequency of the filter. D_p and D_q denote the droop coefficients of the APCL and the RPCL, which are usually determined by the grid code [27]. P_{ref} and Q_{ref} are the active and reactive power references, respectively, and V_{ref} is the rated phase voltage amplitude.

As shown in Fig. 1, the voltage and current inner control loop are usually used to control $\mathbf{V_{pcc}}$ to track the PCC voltage reference, i.e., $\mathbf{V_{pr}} = V_{pr} e^{j\theta_r}$. Since the bandwidth of the inner loop is typically designed to be much higher than that of the outer power loop [28], the inner loop can be regarded as a unity gain. Namely, an ideal PCC voltage reference tracking can be achieved, such that $\mathbf{V_{pcc}} = \mathbf{V_{pr}}$.

B. Mathematical Model of PSC-Controlled Grid-Connected Converter

According to the active and reactive control block diagram in Fig. 1, the phase reference θ_r and amplitude reference V_{pr} for

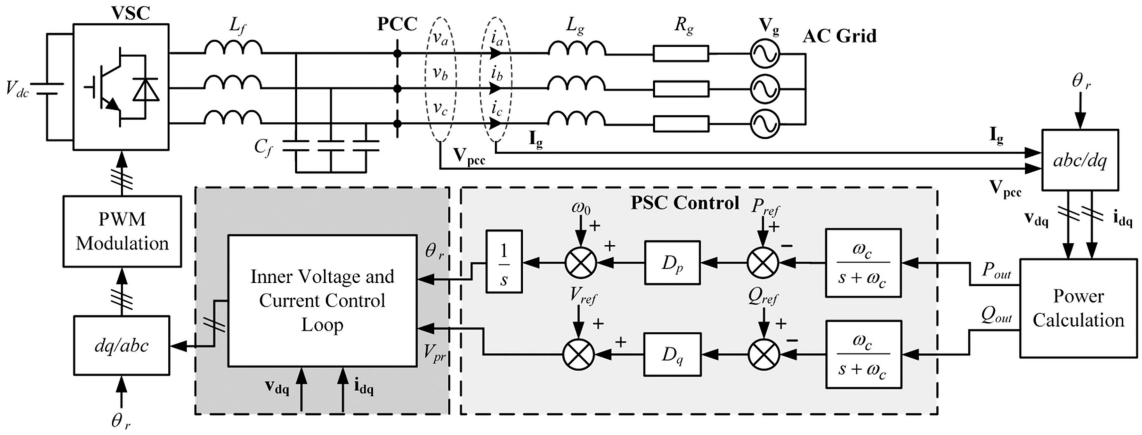

Fig. 1. Structure of a PSC-controlled grid-connected converter.

the PCC voltage can be formulated by

$$\theta_r(s) = \frac{1}{s}\left(\omega_0 + D_p\left(P_{ref} - \frac{\omega_c}{s+\omega_c}P_{out}(s)\right)\right) \quad (1)$$

$$V_{pr}(s) = V_{ref} + D_q\left(Q_{ref} - \frac{\omega_c}{s+\omega_c}Q_{out}(s)\right). \quad (2)$$

To analyze the power dynamics better, both the voltage and current are transformed into a synchronous rotor (dq) frame, and the d-axis is aligned with the grid voltage vector $\mathbf{V_g}$. In this way, the above voltage vectors $\mathbf{V_g}$ and $\mathbf{V_{pcc}}$ in dq frame can be expressed as $\mathbf{V_{gdq}} = V_g$ and $\mathbf{v_{pdq}} = V_{pcc}e^{j\delta_{pcc}}$, respectively, where $\delta_{pcc} = \theta_{pcc} - \omega_g t$ denotes the power angle. The relationship between current and voltage vectors in Fig. 1 can be derived as

$$L_g\frac{d\mathbf{i_{gdq}}}{dt} = \mathbf{v_{pdq}} - V_g - R_g\mathbf{i_{gdq}} - jX_g\mathbf{i_{gdq}} \quad (3)$$

where $X_g = \omega_0 L_g$ is introduced by coordinate transformation [29].

According to (3), the steady-state value of the current vector $\mathbf{I_{gdqe}}$ can be deduced as

$$\mathbf{I_{gdqe}} = \frac{\mathbf{V_{pdqe}} - V_g}{R_g + jX_g} \quad (4)$$

where $\mathbf{V_{pdqe}}$ is the steady-state value of $\mathbf{v_{pdq}}$, i.e., $\mathbf{V_{pdqe}} = V_{pcce}e^{j\delta_{pcce}}$. Around the steady state, a linearization method is performed. Accordingly, the small-signal models of them can be obtained

$$\hat{\mathbf{v}}_{\mathbf{pdq}} = e^{j\delta_{pcce}}\left(\hat{v}_{pcc} + jV_{pcce}\hat{\delta}_{pcc}\right) \quad (5)$$

$$L_g\frac{d\hat{\mathbf{i}}_{\mathbf{gdq}}}{dt} = \hat{\mathbf{v}}_{\mathbf{pdq}} - R_g\hat{\mathbf{i}}_{\mathbf{gdq}} - jX_g\hat{\mathbf{i}}_{\mathbf{gdq}} \quad (6)$$

where cup (^) denotes small signal perturbation.

Applying the Laplace transformation to (6), yields

$$\hat{\mathbf{i}}_{\mathbf{gdq}}(s) = \frac{\hat{\mathbf{v}}_{\mathbf{pdq}}(s)}{sL_g + R_g + jX_g}. \quad (7)$$

The complex power injected into the grid can be calculated by $\mathbf{v_{pdq}}$ and $\mathbf{i_{gdq}}$ as

$$\mathbf{S} = 1.5\mathbf{v_{pdq}}\mathbf{i}^*_{\mathbf{gdq}}. \quad (8)$$

Substituting the steady-state values $\mathbf{V_{pdqe}}$ and $\mathbf{I_{gdqe}}$ into (8), the steady-state power P_e and Q_e can be evaluated as

$$P_e = \frac{3}{2}\frac{\left(V_{pcce}^2 - V_{pcce}V_g\cos\delta_{pcce}\right)R_g + X_gV_{pcce}V_g\sin\delta_{pcce}}{R_g^2 + X_g^2} \quad (9)$$

$$Q_e = \frac{3}{2}\frac{\left(V_{pcce}^2 - V_{pcce}V_g\cos\delta_{pcce}\right)X_g - R_gV_{pcce}V_g\sin\delta_{pcce}}{R_g^2 + X_g^2}. \quad (10)$$

Similarly, by linearizing $\mathbf{S}$ around the steady-state operating point and applying the Laplace transformation, the small-signal model of the complex power is given as

$$\hat{\mathbf{S}}(s) = 1.5\left(\mathbf{V_{pdqe}}\hat{\mathbf{i}}^*_{\mathbf{gdq}}(s) + \hat{\mathbf{v}}_{\mathbf{pdq}}(s)\mathbf{I}^*_{\mathbf{gdqe}}\right). \quad (11)$$

Substituting (4), (5), and (7) into (11), the relationships between $\hat{P}_{out}(s)$, $\hat{Q}_{out}(s)$ and $\hat{V}_{pcc}(s)$, $\hat{\delta}_{pcc}(s)$ in the s-domain can be obtained, respectively, as

$$\begin{cases} K_1(s) = \frac{\hat{P}_{out}(s)}{\hat{\delta}_{pcc}(s)} = \frac{1.5V_{pcce}^2X_g}{(sL_g+R_g)^2+X_g^2} - Q_e \\ K_2(s) = \frac{\hat{Q}_{out}(s)}{\hat{\delta}_{pcc}(s)} = \frac{-1.5V_{pcce}^2(sL_g+R_g)}{(sL_g+R_g)^2+X_g^2} + P_e \\ K_3(s) = \frac{\hat{P}_{out}(s)}{\hat{V}_{pcc}(s)} = \frac{1.5V_{pcce}(sL_g+R_g)}{(sL_g+R_g)^2+X_g^2} + \frac{P_e}{V_{pcce}} \\ K_4(s) = \frac{\hat{Q}_{out}(s)}{\hat{V}_{pcc}(s)} = \frac{1.5V_{pcce}X_g}{(sL_g+R_g)^2+X_g^2} + \frac{Q_e}{V_{pcce}} \end{cases}. \quad (12)$$

Therefore, the small-signal model of the PSC-controlled VSC can be obtained, as shown in Fig. 2. According to (12), the dynamics of the output power are related to the equivalent impedance of the grid as well as the steady-state operating point of the VSC.

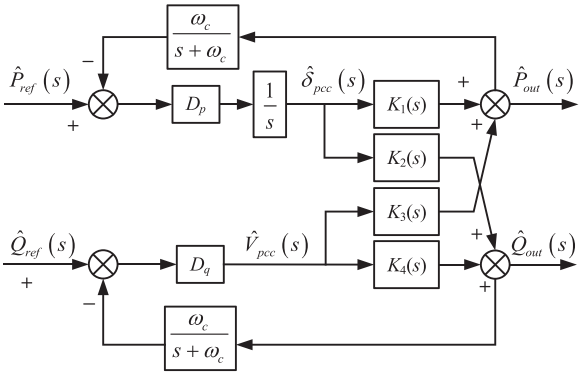

Fig. 2. Small-signal model of the PSC-controlled VSC.

C. Mechanism of Synchronous-Frequency Resonance

Additionally, it can be found that the relationships in (12) all contain a pair of conjugate poles $s_{1,2}$, which are given as

$$s_{1,2} = -R_g/L_g \pm j\omega_0. \tag{13}$$

According to (13), the position of the conjugate poles is determined by the ratio of R_g/L_g.

Moreover, the APCL and RPCL of the VSC are coupled with each other due to $K_2(s)$ and $K_3(s)$, and thereby, it is challenging to control APCL and RPCL independently.

To further analyze the effects of conjugate poles and the coupling effect on the stability of the power control loops, according to Fig. 2, the equivalent loop gains $G_{pc}(s)$ and $G_{qc}(s)$ of the APCL and RPCL are derived as follows:

$$G_{pc}(s) = \frac{D_p\omega_c}{s(s+\omega_c)} \times \left(K_1(s) - \frac{K_2(s)K_3(s)D_q\omega_c/(s+\omega_c)}{1+K_4(s)D_q\omega_c/(s+\omega_c)}\right) \tag{14}$$

$$G_{qc}(s) = \frac{D_q\omega_c}{s+\omega_c} \times \left(K_4(s) - \frac{K_2(s)K_3(s)D_p\omega_c/(s^2+\omega_c s)}{1+K_1(s)D_p\omega_c/(s^2+\omega_c s)}\right). \tag{15}$$

It is obvious that the poles $s_{1,2}$ in (13) are also a pair of conjugate poles for $G_{pc}(s)$ and $G_{qc}(s)$, which introduce a resonance peak and cause $-180°$ phase jump around the synchronous frequency. Thus, a small R_g/L_g will cause a very high resonant peak and might trigger SFR. Meanwhile, the resonant peak will limit the control bandwidth of power control loops, making it hard to be increased above the synchronous frequency when R_g/L_g is small.

In order to filter out high-frequency power fluctuations, the cut-off frequency ω_c of the low pass filter is usually set relatively high, whose impact on SFR can be neglected. Therefore, the influence of D_p and D_q on SFR is analyzed in this article. According to the Nyquist stability criterion, the closed-loop system is stable when $P = R$, where P is the number of open-loop poles in the right half-plane, and R denotes the number of counterclockwise encircled point $(-1, j0)$. According to control theory, the loop gain of the nonminimum phase system has poles or zeros in the right half-plane, which significantly impacts system stability, especially the open-loop poles, as it affects the number of P. To this end, the number of open-loop zeroes in the right half-plane is not a concern. From the Bode diagram, combined amplitude-frequency characteristics with phase-frequency characteristics, the nonminimum phase element can be easily distinguished.

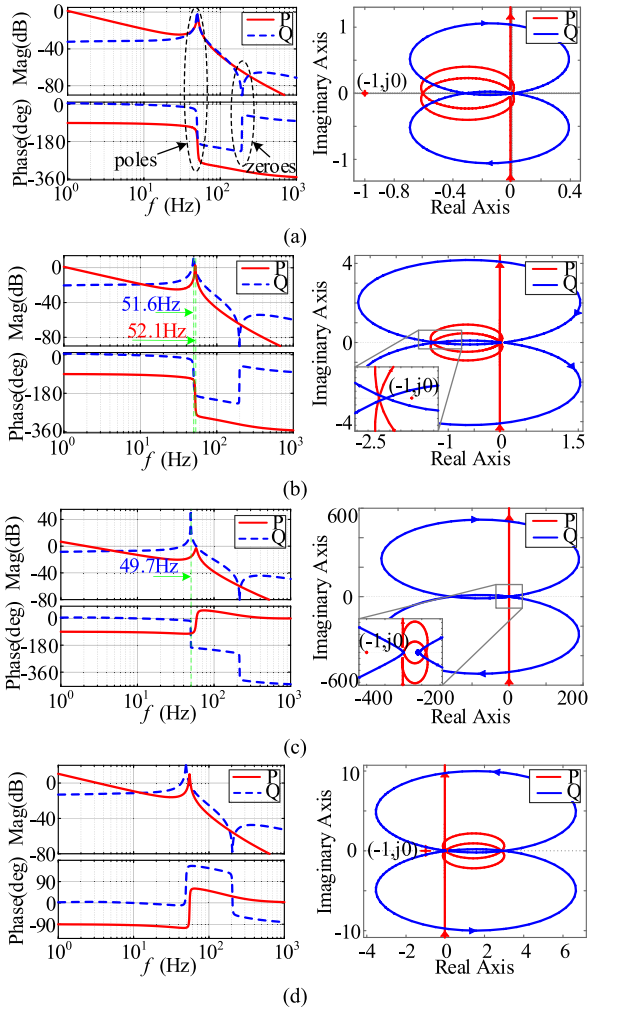

Fig. 3. Bode diagrams and Nyquist plots of $G_{pc}(s)$ and $G_{qc}(s)$ with different D_p and D_q. (a) Stable case: $D_p = 0.01$ p.u., $D_q = 0.01$ p.u. (b) Unstable case (i): $D_p = 0.01$ p.u., $D_q = 0.04$ p.u. (c) Unstable case (ii): $D_p = 0.02$ p.u., $D_q = 0.17$ p.u. (d) Unstable case (iii): $D_p = 0.03$ p.u., $D_q = 0.1$ p.u.

Fig. 3 gives the Bode diagrams, Nyquist curves of $G_{pc}(s)$ and $G_{qc}(s)$ under different droop coefficients. When D_p and D_q are both relatively small, i.e., $D_p = 0.01$ p.u. and $D_q = 0.01$ p.u., as shown in Fig. 3(a), here $P = 0$ and $R = 0$, thus, the system is stable. It can be concluded that a pair of poles cause the resonant peak around the synchronous frequency, while a couple of zeros cause the other resonant peak around 200 Hz, and they are both minimum phase elements. However, the droop coefficients usually selected according to grid code [27] are much higher than 0.01 p.u., which may trigger SFR oscillation.

According to the range of the droop coefficients, the SFR phenomena can be classified into three cases based on the causes that trigger SFR.

1) Unstable case (i): The small equivalent resistance of the inductive network is the main cause of SFR. As shown in Fig. 3(b), $D_p = 0.01$ p.u. and $D_q = 0.04$ p.u. Compared with Fig. 3(a), it can be known that nonminimum phase elements exist in $G_{pc}(s)$ and $G_{qc}(s)$, i.e., $P = 0$. However, the Nyquist curves of $G_{pc}(s)$ and $G_{qc}(s)$ both encircled $(-1, j0)$ point due to the small R_g, such that $R = 2$, triggering an instability. From the Bode diagram, it can be clearly seen that the resonant peak goes over 0 dB around the synchronous frequency where the phase goes below $-180°$, also indicating SFR occurs.
2) Unstable case (ii): The small equivalent resistance R_g and the nonminimum phase are both the causes of SFR. As shown in Fig. 3(c), when $D_p = 0.02$ p.u. and $D_q = 0.17$ p.u., the reactive power loop gain $G_{qc}(s)$ encircled $(-1, j0)$ point due to the small R_g, which trigger SFR for RPCL. Meanwhile, phase lead phenomena of the resonant peak around the synchronous frequency for $G_{pc}(s)$ can be found, indicating that nonminimum elements exist. $P = 2$. $R = 0$ can also be obtained for $G_{pc}(s)$ from the Nyquist curve. Thus, SFR occurs for RPCL due to the nonminimum phase effect. It should be noted that nonminimum elements exist in $G_{qc}(s)$ too, leading to phase lag phenomena for zeros, which does not affect the number of P. A similar case with specific parameters is that the conjugate poles of $G_{pc}(s)$ are near the imaginary axis while the nonminimum phase effect exists in $G_{qc}(s)$ ($P = 2$, $R = 0$).
3) Unstable case (iii): The nonminimum phase effects are the main cause for SFR. As shown in Fig. 3(d), when $D_p = 0.03$ p.u. and $D_q = 1$ p.u. It can be seen that $R = 0$ from the Bode diagram and Nyquist curve, but the system is unstable due to the nonminimum phase effects presented in both $G_{pc}(s)$ and $G_{qc}(s)$, i.e., $P = 2$.

The oscillation frequencies of the SFR triggered by the conjugate poles of $G_{pc}(s)$ and $G_{qc}(s)$ are marked with green dashed lines in the Bode diagram of Fig. 3, which is around the synchronous frequency. The oscillation frequency corresponding to the nonminimum phase effect cannot be identified directly through the Bode diagram or Nyquist curve, but can be calculated by substituting the actual parameters into $G_{pc}(s)$ and $G_{qc}(s)$, which is calculated between 49.5 and 58 Hz for Fig. 3(c) and (d). In summary, the oscillation frequencies correspond to the small equivalent resistance R_g and the nonminimum phase effect are both around the synchronous frequency, resulting in the unstable phenomena presented as SFR.

More unstable cases and corresponding P and R under a wider range of droop coefficients are summarized in Table I. From them, it can be clearly found that the small equivalent resistance of the inductive network is one main cause for SFR, as it leads to a very high resonance peak and causes $-180°$ phase jump around synchronous frequency in open-loop gains, which has been pointed out in [25]. Further investigations in this article found that the existence of the nonminimum phase elements in $G_{pc}(s)$ and $G_{qc}(s)$ are another important root cause. Sometimes, the SFR is even triggered by a combination of the two causes, one is in the APCL and the other occurs in RPCL.

TABLE I
STABILITY OF PSC-CONTROLLED GRID-CONNECTED CONVERTER UNDER DIFFERENT D_p AND D_q

Stability	Droop coefficients		Basis of stability evaluation	
	D_p /p.u.	D_q /p.u.	APCL	RPCL
Stable	(0,0.02)	(0,0.03)	$P = 0, R = 0$	$P = 0, R = 0$
Unstable case (i)	(0,0.02)	(0.03,0.07)	$P = 0, R = 2$	$P = 0, R = 2$
Unstable case (ii)	(0.02,0.5)	(0,0.07)	$P = 0, R = 2$	$P = 2, R = 0$
	(0,0.02)	(0.07,0.9)	$P = 2, R = 0$	$P = 0, R = 2$
	(0.02,0.03)	(0.1,0.9)		
Unstable case (iii)	(0.02,0.03)	(0.07,0.1)	$P = 2, R = 0$	$P = 2, R = 0$
	(0.03,0.5)	(0.07,0.9)		

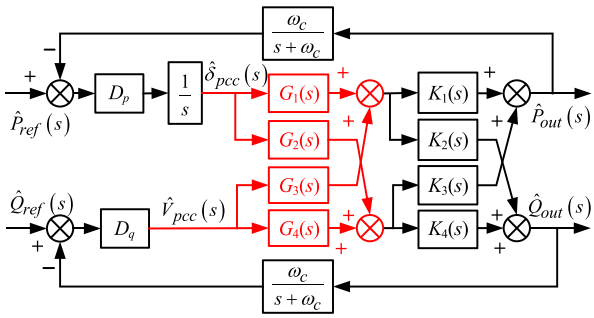

Fig. 4. Topology of the proposed auxiliary branches in the small-signal model.

III. SUPPRESSION STRATEGY FOR SFR OF PSC-CONTROLLED GRID-CONNECTED CONVERTERS

A. Conjugate Poles Elimination Control Method Is Proposed

To solve the above issues, a conjugate poles elimination control method is proposed to suppress the SFR, which is based on the auxiliary branches $G_1(s)$, $G_2(s)$, $G_3(s)$, and $G_4(s)$ introduced into the power control loops in Fig. 2, as shown in Fig. 4. From it, after applying the auxiliary branches, the relationships between $\hat{P}_{out}(s)$, $\hat{Q}_{out}(s)$ and $\hat{V}_{pcc}(s)$, $\hat{\delta}_{pcc}(s)$ can be derived as

$$\begin{aligned}\begin{bmatrix}\hat{P}_{out}(s)\\ \hat{Q}_{out}(s)\end{bmatrix} &= \underbrace{\begin{bmatrix}K_1(s) & K_3(s)\\ K_2(s) & K_4(s)\end{bmatrix}}_{\boldsymbol{K}(s)}\underbrace{\begin{bmatrix}G_1(s) & G_3(s)\\ G_2(s) & G_4(s)\end{bmatrix}}_{\boldsymbol{G}(s)}\\ &\quad\times\begin{bmatrix}\hat{\delta}_{pcc}(s)\\ \hat{V}_{pcc}(s)\end{bmatrix}\\ &= \underbrace{\begin{bmatrix}K'_1(s) & K'_3(s)\\ K'_2(s) & K'_4(s)\end{bmatrix}}_{\boldsymbol{K}'(s)}\begin{bmatrix}\hat{\delta}_{pcc}(s)\\ \hat{V}_{pcc}(s)\end{bmatrix}\end{aligned} \tag{16}$$

where $\boldsymbol{K}(s)$ denotes the relationship matrix between $\widehat{P}_{out}(s)$, $\widehat{Q}_{out}(s)$ and $\widehat{V}_{pcc}(s)$, $\widehat{\delta}_{pcc}(s)$ in the small-signal model of the

original system. $\boldsymbol{G}(s)$ is the transfer function matrix of the auxiliary branches, and $\boldsymbol{K}'(s)$ is regarded as the equivalent relationship transfer function matrix after applying the auxiliary branches.

According to (16), a desirable $\boldsymbol{G}(s)$ is required to eliminate the conjugate poles in each item of $\boldsymbol{K}(s)$. Moreover, $G_1(s) = G_4(s) = 1$ is considered, making the structure of the additional auxiliary branches as simple as possible. Take the derivation process of $G_2(s)$ as an example, which is contained in $K'_1(s)$ and $K'_2(s)$. Expanding and simplifying $K'_1(s)$ and $K'_2(s)$ further as (17) and (18) shown at bottom of this page, according to which, to eliminate the conjugate poles in K_1'(s) and K_2'(s), $G_2(s)$ may not be unique. Note that (17) and (18) are shown at the bottom of this page. In this article, we only focus on the two simplest solutions that can be deduced directly as

$$G_2(s) = V_{pcce}\frac{sL_g + R_g}{X_g} = V_{pcce}\frac{s + R_g/L_g}{\omega_0}. \tag{19}$$

Similarly, $G_3(s)$ can be deduced by expanding $K'_3(s)$ and $K'_4(s)$ further, which can be derived as

$$G_3(s) = -\frac{1}{V_{pcce}}\frac{sL_g + R_g}{X_g} = -\frac{1}{V_{pcce}}\frac{s + R_g/L_g}{\omega_0}. \tag{20}$$

In this way, substituting (19) and (20) into (16), the elements of $\boldsymbol{K}'(s)$ can be obtained as follows:

$$\begin{cases} K'_1(s) = \frac{1.5V_{pcce}^2}{X_g} - Q_e + \frac{sL_g+R_g}{X_g}P_e \\ K'_2(s) = P_e + \frac{sL_g+R_g}{X_g}Q_e \\ K'_3(s) = \frac{P_e}{V_{pcce}} + \frac{sL_g+R_g}{X_g}\frac{Q_e}{V_{pcce}} \\ K'_4(s) = \frac{1.5V_{pcce}}{X_g} + \frac{Q_e}{V_{pcce}} - \frac{sL_g+R_g}{X_g}\frac{P_e}{V_{pcce}}. \end{cases} \tag{21}$$

Obviously, no conjugate poles can be found in K_1'(s), K_2'(s), K_3'(s), or K_4'(s). Particularly, when the system operates in a low power condition, such as P_e and Q_e are extremely small, K_2'(s) ≈ 0 and K_3'(s) ≈ 0 can be derived from (21). Under this condition, it can be considered that the APCL and RPCL are decoupled completely from each other, thus, they can be controlled independently.

According to the small-signal model in Fig. 4, the proposed auxiliary branches can be implemented in the control method as shown in Fig. 5.

B. Advantages of Conjugate Poles Elimination Control Method

When the auxiliary branches are introduced, the loop gains of APCL and RPCL can be rewritten by combining (21), (14), and (15). Namely, replacing $K_1(s)$ - $K_4(s)$ with K_1'(s) - K_4'(s) in $G_{pc}(s)$ and $G_{qc}(s)$, based on which, the Bode diagrams are plotted in Fig. 6. To investigate the normal operation of VSC, the D_p and D_q are the same as in the unstable case (ii), i.e., D_p

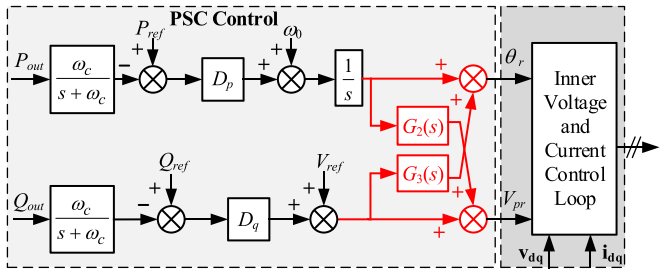

Fig. 5. Implementation for the proposed auxiliary branches in the control diagram.

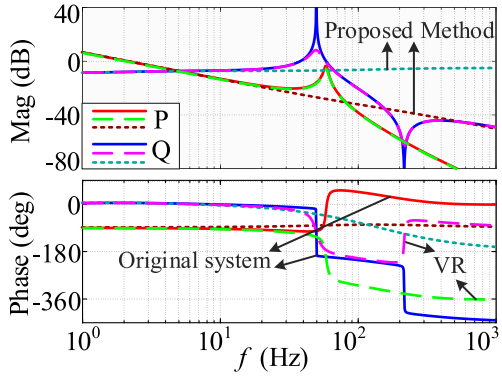

Fig. 6. Bode diagrams of $G_{pc}(s)$ and $G_{qc}(s)$ with the proposed auxiliary branches or VR employed in the original system with cut-off frequency f_c = 2 Hz.

$= 0.02$ p.u. and $D_q = 0.17$ p.u. From Fig. 6, it can be found that the phase lag of $-180°$ introduced by the conjugate poles in $G_{qc}(s)$ is eliminated by the proposed method. Meanwhile, the nonminimum phase is also removed from $G_{pc}(s)$ thus the SFR is suppressed. To conclude, the auxiliary branches introduced in this article can not only eliminate the resonant poles in $G_{pc}(s)$ and $G_{qc}(s)$, but can also remove the nonminimum phase effect in them. Therefore, both the two causes of SFR are completely suppressed, and the stability of the system is greatly improved.

Usually, to dampen the SFR in PSC-controlled VSC, a conventional method is to employ a VR R_v. Fig. 6 also gives the Bode diagrams of $G_{pc}(s)$ and $G_{qc}(s)$ with $R_v = 0.03$ p.u., where the VR can effectively damp the resonance peak in $G_{qc}(s)$. However, due to the phase lag of $-180°$ in $G_{qc}(s)$ is not removed, the SFR may probably be triggered when the system bandwidth increases.

In the original system, the bandwidth cannot be set too high due to the limitation of the resonant peaks of $G_{pc}(s)$ and $G_{qc}(s)$. When the cut-off frequency f_c of $G_{pc}(s)$ is 2 Hz, for instance, the system is unstable, and it is required to reduce D_p further to reduce the cut-off frequency, as shown in the stable case

$$K'_1(s) = K_1(s) + G_2(s)K_3(s) = \frac{1.5V_{pcce}}{sL_g + R_g}\left(G_2(s) - X_g^2\frac{G_2(s) - V_{pcce}(sL_g + R_g)/X_g}{(sL_g + R_g)^2 + X_g^2}\right) + G_2(s)\frac{P_e}{V_{pcce}} - Q_e \tag{17}$$

$$K'_2(s) = K_2(s) + G_2(s)K_4(s) = 1.5V_{pcce}X_g\frac{G_2(s) - V_{pcce}(sL_g + R_g)/X_g}{(sL_g + R_g)^2 + X_g^2} + G_2(s)\frac{Q_e}{V_{pcce}} + P_e \tag{18}$$

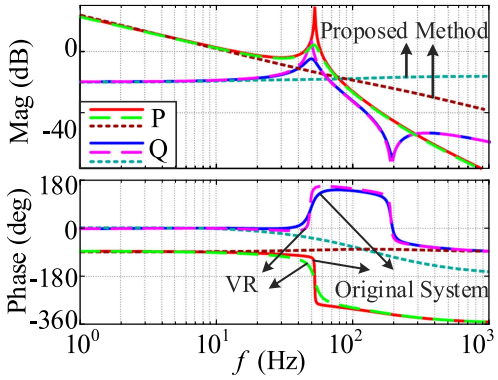

Fig. 7. Bode diagrams of $G_{pc}(s)$ and $G_{qc}(s)$ with the proposed auxiliary branches or VR when cut-off frequency $f_c = 12$ Hz.

in Fig. 3(a). Fortunately, with the proposed auxiliary branches, which eliminate the resonance peaks of $G_{pc}(s)$ and $G_{qc}(s)$, the phase lag of $-180°$ in $G_{pc}(s)$ and $G_{qc}(s)$ no longer exists. Therefore, this method is able to broaden the bandwidth and improve the response dynamics. Although employing an R_v can suppress the SFR when $f_c = 2$ Hz, the oscillation will inevitably occur as long as the bandwidth is increased to some extent. For example, when f_c is increased to 12 Hz ($D_p = 0.09$ p.u. and $D_q = 0.01$ p.u.), as shown in Fig. 7, although $R_v = 0.03$ p.u. is employed, the resonance peak of $G_{pc}(s)$ will still trigger the SFR. Nevertheless, when $f_c = 12$ Hz, the system with the proposed auxiliary branches satisfies the Nyquist stability criterion and will be kept stable.

Noting that, we do not know the grid resistance R_g and L_g in advance in the practice. Thus, it is hard to design the auxiliary branches using the accurate R_g and L_g parameters. However, SFR can be triggered by a small ratio of R_g/L_g, thus, the worst-case can be considered to design the parameters for pole-zero cancellation method. Fortunately, the ratio of R_g/L_g is in a specific range for the specific grid lines [9]. Of course, with the worst-case designing for $G_2(s)$ and $G_3(s)$, which cannot perfectly achieve pole-zero cancellation, it can still greatly dampen the resonant peak for the worst-case and stabilize the system. For other scenarios, the proposed method can provide a higher damping ratio around the synchronous frequency, and it can surely suppress SFR.

C. Simplification of the Proposed Strategy Under Different Situations

It should be noted that the steady-state voltage V_{pcce} is necessary for deriving the auxiliary branches $G_2(s)$ and $G_3(s)$, which usually fluctuate in a small range. To facilitate practical applications, instead, the rated voltage amplitude V_{ref} can be used. Thus, the auxiliary branches are simplified to

$$G_2(s) = V_{ref}\frac{s + R_g/L_g}{\omega_0} \tag{22}$$

$$G_3(s) = -\frac{1}{V_{ref}}\frac{s + R_g/L_g}{\omega_0}. \tag{23}$$

TABLE II
CHARACTERISTICS OF THE PROPOSED AUXILIARY BRANCHES UNDER DIFFERENT SIMPLIFIED CONDITIONS

Simplified Conditions	Auxiliary Branches		Features
	$G_2(s)$	$G_3(s)$	
No Simplification	$V_{pcce}\frac{s+R_g/L_g}{\omega_0}$	$-\frac{1}{V_{pcce}}\frac{s+R_g/L_g}{\omega_0}$	•Eliminate the conjugate poles. •Broaden the power bandwidth.
Small Power Condition $\delta \approx 0$	$V_{ref}\frac{s+R_g/L_g}{\omega_0}$	$-\frac{1}{V_{ref}}\frac{s+R_g/L_g}{\omega_0}$	•Decouple the power control loops. •Eliminate the conjugate poles. •Broaden the power bandwidth.
Inductive system $R_g \approx 0$	$V_{ref}\frac{s}{\omega_0}$	$-\frac{1}{V_{ref}}\frac{s}{\omega_0}$	•Eliminate the conjugate poles. •Broaden the power bandwidth.

The corresponding $\boldsymbol{K}'(s)$ with the simplified auxiliary branches can be deduced by substituting (22) and (23) into (16), and the Bode diagrams of $G_{pc}(s)$ and $G_{qc}(s)$ can be obtained according to (14) and (15), which is found to almost coincide with the Bode diagrams when V_{pcce} is applied.

For a very high-voltage network, the R_g is much smaller than L_g, which can be neglected. Thus, the corresponding auxiliary branches $G_2'(s)$ and $G_3'(s)$ are simplified to be

$$G'_2(s) = V_{ref}\frac{s}{\omega_0} \tag{24}$$

$$G'_3(s) = -\frac{1}{V_{ref}}\frac{s}{\omega_0}. \tag{25}$$

To summarize, the expressions and characteristics of the proposed auxiliary branches under various simplified conditions above are compared in Table II. It should be pointed out that, $G_2(s)$ and $G_3(s)$ here contain differential terms, which are usually difficult to be realized in practice, as the high-frequency noise can be amplified. Fortunately, LPFs are usually added to filter out the high-frequency noise for the output power, i.e., P_{out} and Q_{out}, as shown in Fig. 5, which can eliminate the effect of differential terms in $G_2(s)$ and $G_3(s)$ for high-frequency noise. Moreover, the integral term in APCL can completely cancel out the differential term in $G_2(s)$. Thus, the differential terms in $G_2(s)$ and $G_3(s)$ in this article can be realized without extra changes.

IV. Simulation and Experimental Verification

A. Simulation and Experimental Verification of SFR

To verify the theoretical mechanism analysis of SFR, a PSC-controlled grid-connected converter is built in Simulink/MATLAB. The main parameters of the studied system are given in Table III.

TABLE III
MAIN PARAMETERS OF THE PSC SYSTEM

Parameters	Value	Parameters	Value
Rated power S_{ref}	1.6 MVA	Short circuit ratio (SCR)	2.5
Rated active power P_{ref}	1.0 p.u.	Rated frequency f_0	50 Hz
Rated power Q_{ref}	0	Rated angular frequency ω_0	$2\pi f_0$
Rated voltage (Phase Amplitude) V_{ref}	563 V	Droop coefficient of P-f D_p	0.02 ω_0/S_{ref}
Grid voltage (L-L RMS)	590 V	Droop coefficient of Q-V D_q	0.17 V_{ref}/S_{ref}
Grid inductance L_g	0.4 p.u.	Virtual resistor R_v	0.03 p.u.
Grid resistor R_g	0.009 p.u.	Filter cut-off frequency ω_c	320π *rad/s*

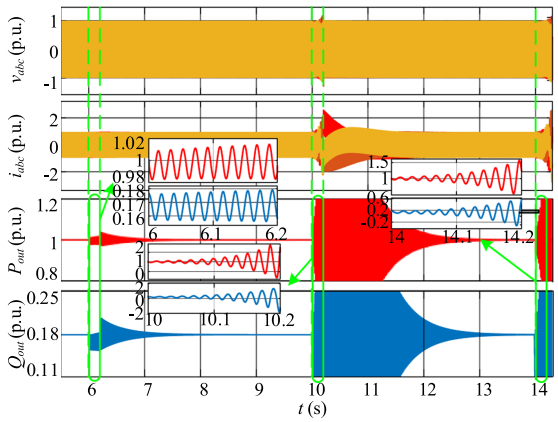

Fig. 8. Simulation waveforms of v_{abc}, i_{abc}, P_{out}, Q_{out} with different droop coefficients.

The stable and three unstable cases in Section II are verified through simulation results, as shown in Fig. 8. The system starts up with the stable case, i.e., $D_p = 0.01$ p.u. and $D_q = 0.01$ p.u. as shown in Fig. 3(a), and the system keeps stable. During the three intervals, such as t = 6–6.2 s, t = 10–10.2 s, and t = 14 s, the paraments are switched to the unstable case (i) (i.e., $D_p = 0.01$ p.u., $D_q = 0.04$ p.u.), unstable case (ii) (i.e., $D_p = 0.02$ p.u., $D_q = 0.17$ p.u.), and unstable case (iii) (i.e., $D_p = 0.03$ p.u., $D_q = 0.1$ p.u.), respectively. Of course, the system becomes unstable during these intervals. The parameters are changed back to the stable case at t = 6.2 s and t = 10.2 s, and accordingly, the oscillation can be removed and the system gradually becomes stable. From Fig. 8, it is obvious that SFR is triggered at t = 6, 10, and 14 s. The oscillation waveforms of the three intervals were analyzed by fast Fourier (FFT) analysis and the results are shown in Fig. 9 , where the main oscillation frequencies are approximately equal to synchronous frequency, which agrees well with the theoretical analysis in Fig. 3.

Furthermore, a control hardware-in-the-loop experimental setup as shown in Fig. 10, which is based on a DSP+FPGA control board and RT-LAB real-time digital simulation platform,

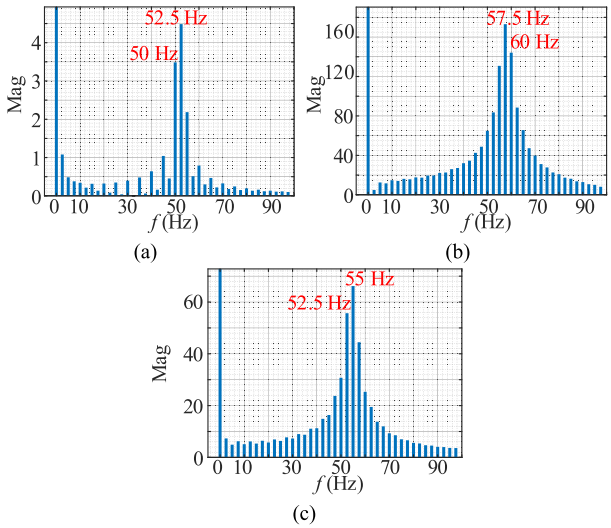

Fig. 9. FFT analysis of oscillation waveform. (a) 6–6.2 s. (b) 10–10.2 s. (c) 14–14.2 s.

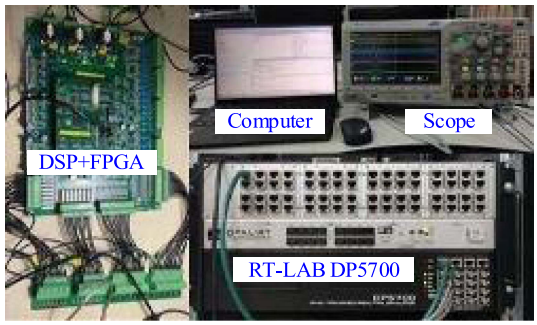

Fig. 10. Control hardware-in-the-loop experiment platform.

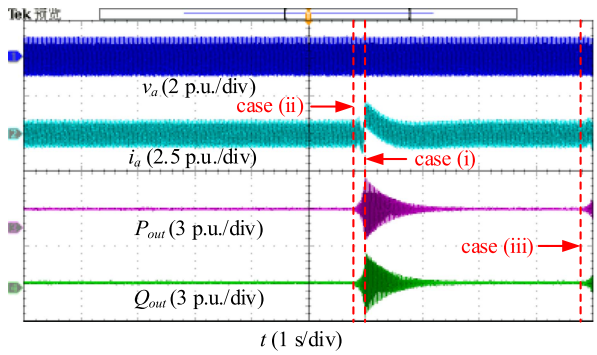

Fig. 11. Experimental waveforms of v_a, i_a, P_{out}, Q_{out} with different droop coefficients.

is built and implemented in the laboratory. To validate some of the unstable cases in Section II, the system starts up with parameters of the stable case, thus the system is stable at the beginning. Then, the control parameters are changed to the unstable case (ii), and quickly switch to the stable case. When the system gradually returns to become stable, the parameters are changed again to the unstable case (iii). The corresponding experimental waveforms are shown in Fig. 11. It can clearly be seen that the oscillation occurs when the system switches

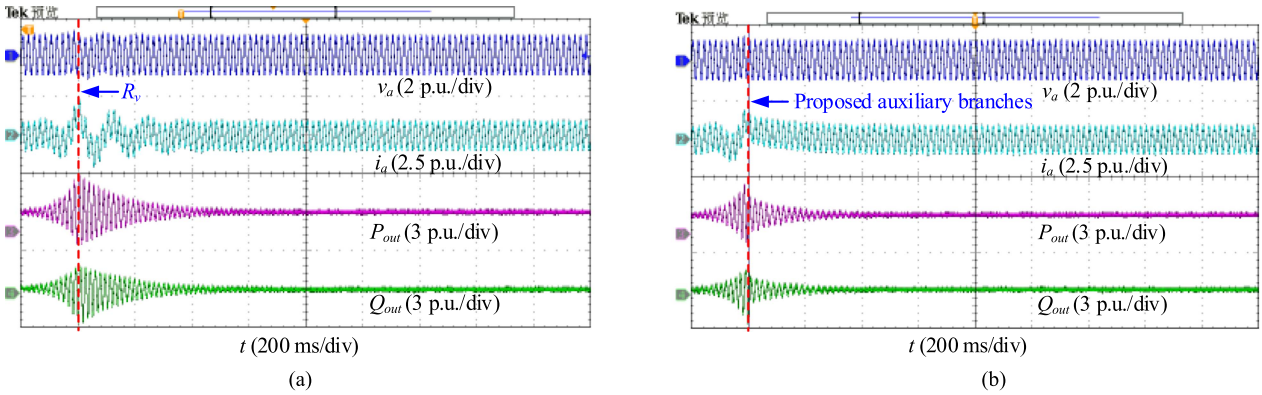

Fig. 12. Experimental waveforms of v_a, i_a, P_{out}, Q_{out} under the original system. (a) Using R_v. (b) Using proposed auxiliary branches.

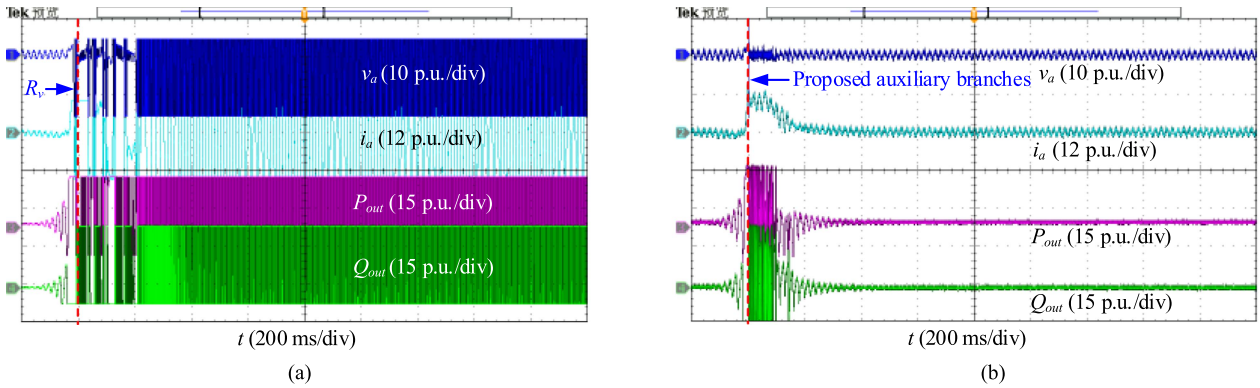

Fig. 13. Experimental waveforms of v_a, i_a, P_{out}, Q_{out} with $G_{pc}(s)$ cut-off frequency increased to 12 Hz. (a) Using R_v. (b) Using proposed auxiliary branches.

to unstable case (ii) and unstable case (iii), which is consistent with the corresponding theoretical analysis and simulation results, which verify that both the small equivalent resistance R_g and the nonminimum phase effect may trigger the SFR in the PSC-controlled grid-connected converter.

B. Experimental Validation of the Proposed Method

To further verify the effectiveness of the proposed conjugate poles elimination control method, experiments are also carried out in control hardware-in-the-loop experimental platform.

When the system is stable, the droop coefficients are changed to the usually designed one according to the grid code, i.e., the unstable case (ii). Obviously, the system becomes unstable. Quickly, the VR $R_v = 0.03$ p.u. or the proposed auxiliary branches are added into the control loop, the experimental results are shown in Fig. 12. From them, it can be seen that it takes about 0.8 s to achieve a steady state after applying the VR, while the SFR is eliminated within 0.6 s with a smaller overshoot after applying the auxiliary branches. Obviously, the proposed conjugate poles elimination control method is more efficient than the conventional VR strategy.

In order to further validate the performance of the two methods under higher bandwidths, the parameters are adjusted to increase the open-loop cut-off frequency to 12 Hz. A VR $R_v = 0.03$ p.u. or the proposed auxiliary branches are separately applied after the system becomes unstable, as shown in Fig. 13. From them, it can be seen that the system is unstable even when using the VR method, which also corresponds to the theoretical analysis in Fig. 7. In contrast, the SFR in Fig. 12(b) will be effectively dampened after employing the auxiliary branches as proposed in this article.

The above experimental results prove that the proposed conjugate poles elimination control method has better adaptability than the traditional VR method, and it can effectively improve the response dynamics of the system by broadening the control bandwidth.

V. Conclusion

Based on the small-signal model of PSC-controlled converter by considering the dynamics of the equivalent inductance of the grid, the mechanism of SFR for PSC-controlled converter is investigated thoroughly in this article. It is revealed that not only the small equivalent resistance of the inductive network but also the existence of the nonminimum phase effect of the loop gain is the main cause of SFR. Particularly, the effects of different droop coefficients on the system stability are studied, and it is demonstrated that the nonminimum phase effect may lead to SFR independently. In addition, a conjugate poles elimination control method based on auxiliary branches introduced into the power control loops is proposed to suppress SFR. This method

can not only eliminate the conjugate poles in open-loop gain but also remove the nonminimum phase elements. Meanwhile, the control bandwidth is broadened, which effectively improves the response dynamics of the system and it has better adaptability compared with the traditional VR method. Finally, simulation and hardware-in-loop experimental results are implemented to validate the theoretical analysis and the effectiveness of the proposed method.

REFERENCES

[1] F. Blaabjerg, Y. Yang, D. Yang, and X. Wang, "Distributed power-generation systems and protection," *Proc. IEEE*, vol. 105, no. 7, pp. 1311–1331, Jul. 2017.

[2] C. Arghir and F. Dörfler, "The electronic realization of synchronous machines: Model matching, angle tracking, and energy shaping techniques," *IEEE Trans. Power Electron.*, vol. 35, no. 4, pp. 4398–4410, Apr. 2020.

[3] W. Gong, S. Hu, M. Shan, and H. Xu, "Robust current control design of a three phase voltage source converter," *J. Modern Power Syst. Clean Energy*, vol. 2, no. 1, pp. 16–22, Mar. 2014.

[4] H. Yuan, X. Yuan, and J. Hu, "Modeling of grid-connected VSCS for power system small-signal stability analysis in DC-link voltage control timescale," *IEEE Trans. Power Syst.*, vol. 32, no. 5, pp. 3981–3991, Sep. 2017.

[5] B. Wen, D. Dong, D. Boroyevich, R. Burgos, P. Mattavelli, and Z. Shen, "Impedance-based analysis of grid-synchronization stability for three-phase paralleled converters," *IEEE Trans. Power Electron.*, vol. 31, no. 1, pp. 26–38, Jan. 2016.

[6] J. Z. Zhou, H. Ding, S. Fan, Y. Zhang, and A. M. Gole, "Impact of short-circuit ratio and phase-locked-loop parameters on the small-signal behavior of a VSC-HVDC converter," *IEEE Trans. Power Del.*, vol. 29, no. 5, pp. 2287–2296, Oct. 2014.

[7] H. Wu et al., "Small-signal modeling and parameters design for virtual synchronous generators," *IEEE Trans. Ind. Electron.*, vol. 63, no. 7, pp. 4292–4303, Jul. 2016.

[8] F. M. Hughes, O. Anaya-Lara, N. Jenkins, and G. Strbac, "Control of DFIG-based wind generation for power network support," *IEEE Trans. Power Syst.*, vol. 20, no. 4, pp. 1958–1966, Nov. 2005.

[9] J. Rocabert, A. Luna, F. Blaabjerg, and P. Rodríguez, "Control of power converters in AC microgrids," *IEEE Trans. Power Electron.*, vol. 27, no. 11, pp. 4734–4749, Nov. 2012.

[10] A. González-Cajigas, J. Roldán-Pérez, and E. J. Bueno, "Design and analysis of parallel-connected grid-forming virtual synchronous machines for Island and grid-connected applications," *IEEE Trans. Power Electron.*, vol. 37, no. 5, pp. 5107–5121, May 2022.

[11] C. Li, Y. Yang, Y. Cao, A. Aleshina, J. Xu, and F. Blaabjerg, "Grid inertia and damping support enabled by proposed virtual inductance control for grid-forming virtual synchronous generator," *IEEE Trans. Power Electron.*, vol. 38, no. 1, pp. 294–303, Jan. 2023.

[12] L. Huang, H. Xin, and Z. Wang, "Damping low-frequency oscillations through VSC-HVDC stations operated as virtual synchronous machines," *IEEE Trans. Power Electron.*, vol. 34, no. 6, pp. 5803–5818, Jun. 2019.

[13] X. Xiong, C. Wu, B. Hu, D. Pan, and F. Blaabjerg, "Transient damping method for improving the synchronization stability of virtual synchronous generators," *IEEE Trans. Power Electron.*, vol. 36, no. 7, pp. 7820–7831, Jul. 2021.

[14] X. Xiong, C. Wu, and F. Blaabjerg, "An improved synchronization stability method of virtual synchronous generators based on frequency feedforward on reactive power control loop," *IEEE Trans. Power Electron.*, vol. 36, no. 8, pp. 9136–9148, Aug. 2021.

[15] L. Zhang, L. Harnefors, and H.-P. Nee, "Power-synchronization control of grid-connected voltage-source converters," *IEEE Trans. Power Syst.*, vol. 25, no. 2, pp. 809–820, May 2010.

[16] L. Harnefors, F. M. M. Rahman, M. Hinkkanen, and M. Routimo, "Reference-feedforward power-synchronization control," *IEEE Trans. Power Electron.*, vol. 35, no. 9, pp. 8878–8881, Sep. 2020.

[17] A. Sepehr, O. Gomis-Bellmunt, and E. Pouresmaeil, "Employing machine learning for enhancing transient stability of power synchronization control during fault conditions in weak grids," *IEEE Trans. Smart Grid*, vol. 13, no. 3, pp. 2121–2131, May 2022.

[18] L. Zhang, L. Harnefors, and H.-P. Nee, "Interconnection of two very weak AC systems by VSC-HVDC links using power-synchronization control," *IEEE Trans. Power Syst.*, vol. 26, no. 1, pp. 344–355, Feb. 2011.

[19] A. A. A. Radwan and Y. A.-R. I. Mohamed, "Power synchronization control for grid-connected current-source inverter-based photovoltaic systems," *IEEE Trans. Energy Convers.*, vol. 31, no. 3, pp. 1023–1036, Sep. 2016.

[20] S. I. Nanou and S. A. Papathanassiou, "Grid code compatibility of VSC-HVDC connected offshore wind turbines employing power synchronization control," *IEEE Trans. Power Syst.*, vol. 31, no. 6, pp. 5042–5050, Nov. 2016.

[21] L. Zhang, H.-P. Nee, and L. Harnefors, "Analysis of stability limitations of a VSC-HVDC link using power synchronization control," *IEEE Trans. Power Syst.*, vol. 26, no. 3, pp. 1326–1337, Aug. 2011.

[22] J. Wang, Y. Wang, Y. Gu, W. Li, and X. He, "Synchronous frequency resonance of virtual synchronous generators and damping control," in *Proc. 9th Int. Conf. Power Electron. Asia*, 2015, pp. 1011–1016.

[23] J. Fang, H. Li, Y. Tang, and F. Blaabjerg, "Distributed power system virtual inertia implemented by grid-connected power converters," *IEEE Trans. Power Electron.*, vol. 33, no. 10, pp. 8488–8499, Oct. 2018.

[24] C. Li, S. K. Chaudhary, M. Savaghebi, J. C. Vasquez, and J. M. Guerrero, "Power flow analysis for low-voltage AC and DC microgrids considering droop control and virtual impedance," *IEEE Trans. Smart Grid*, vol. 8, no. 6, pp. 2754–2764, Nov. 2017.

[25] D. Yang, H. Wu, X. Wang, and F. Blaabjerg, "Suppression of synchronous resonance for VSGs," *J. Eng.*, vol. 2017, no. 13, pp. 2574–2579, 2017.

[26] X. Xiong, C. Wu, and F. Blaabjerg, "Effects of virtual resistance on transient stability of virtual synchronous generators under grid voltage droop," *IEEE Trans. Ind. Electron.*, vol. 69, no. 5, pp. 4754–4764, May 2022.

[27] *Requirements for the connection of micro generators in parallel with public low-voltage distribution networks*, CENELEC Standard EN 50438, 2008.

[28] L. Harnefors, X. Wang, A. G. Yepes, and F. Blaabjerg, "Passivity-based stability assessment of grid-connected VSCS—An overview," *IEEE J. Emerg. Sel. Topics Power Electron.*, vol. 4, no. 1, pp. 116–125, Mar. 2016.

[29] H. Akagi, E. H. Watanabe, and M. Aredes, "The instantaneous power theory," in *Instantaneous Power Theory and Applications to Power Conditioning*. Hoboken, NJ, USA: Wiley, 2017, ch. 3, pp. 37–10.

Xiaoling Xiong (Member, IEEE) received the B.S., M.S., and Ph.D. degrees in electrical engineering from the Nanjing University of Aeronautics and Astronautics, Nanjing, China, in 2007, 2010, and 2015, respectively.

From February 2011 to July 2012, she was a Research Assistant with the Department of Electronic and Information Engineering, Hong Kong Polytechnic University, Hong Kong. Since 2015, she has been with North China Electric Power University, Beijing, China, where she is currently an Associate Professor. Simultaneously, she has been with Aalborg University, Aalborg, Denmark, where she was a visiting Postdoctoral with the Department of Energy Technology from December 2018 to November 2020. Her current research interests include HVdc system, modeling, analysis and design power electronic systems, and study the nonlinear behaviors in power electronic circuits.

Yan Zhou received the B.S. degree in electrical engineering and its automation from the North China Electric Power University, Baoding, China, in 2020. She is currently working toward the M.S. degree majoring in electrical engineering with the Department of Electrical and Electronic Engineering, North China Electric Power University, Beijing, China.

Her research interests include modeling, analysis, and design of grid-forming VSC.

Bochen Luo was born in Hunan, China. He received the B.S. degree in electrical engineering from the Changsha University of Science and Technology, Changsha, China, in 2021. He is currently working toward the M.S. degree majoring in electrical engineering with the Department of Electrical and Electronic Engineering, North China Electric Power University, Beijing, China.

His research interests include modeling, analysis, and design of converter-based power systems.

Peng Cheng (Member, IEEE) was born in Liaoning Province, China. He received the B.S. and Ph.D. degrees from Zhejiang University, Hangzhou, China, in 2011 and 2016, both in electrical engineering.

He is currently an Assistant Professor with the Department of China Institute of Energy and Transport Integration Development, North China Electric Power University, China. His current research interests include renewable energy-integrated transportation, and multiconverter power systems.

Frede Blaabjerg (Fellow, IEEE) received the Ph.D. degree in electrical engineering from the Aalborg University, Aalborg, Denmark, in 1995.

From 1987 to 1988, he was with ABB-Scandia, Randers, Denmark. He became an Assistant Professor, in 1992, an Associate Professor, in 1996, and a Full Professor of power electronics and drives, in 1998, with AAU EnergyAalborg, Denmark. In 2017, he became a Villum Investigator. He was Honoris Causa with the University Politehnica Timisoara (UPT), Timisoara, Romania, in 2017 and Tallinn Technical University (TTU), Tallinn, Estonia, in 2018. He has authored or coauthored more than 600 journal papers in the fields of power electronics and its applications. He is the coauthor of four monographs and the Editor of ten books in power electronics and its applications. His current research interests include power electronics and its applications, such as in wind turbines, PV systems, reliability, harmonics, and adjustable speed drives.

Dr. Blaabjerg was the recipient of 38 IEEE Prize Paper Awards, the IEEE PELS Distinguished Service Award in 2009, EPE-PEMC Council Award in 2010, IEEE William E. Newell Power Electronics Award 2014, Villum Kann Rasmussen Research Award 2014, Global Energy Prize in 2019, and 2020 IEEE Edison Medal. He was the Editor-in-Chief of the IEEE TRANSACTIONS ON POWER ELECTRONICS from 2006 to 2012. He has been a Distinguished Lecturer for the IEEE Power Electronics Society from 2005 to 2007 and for the IEEE Industry Applications Society from 2010 to 2011 and 2017 to 2018. In 2019–2020, he was the President of IEEE Power Electronics Society. He has been the Vice-President of the Danish Academy of Technical Sciences. He was nominated in 2014–2021 by Thomson Reuters to be among the most 250 cited researchers in engineering worldwide.